Understanding the Role of Underlayers and Overlayers in Thin Film Hematite Photoanodes

Ludmilla Steier, Isaac Herraiz-Cardona, Sixto Gimenez, Francisco Fabregat-Santiago, Juan Bisquert, S. David Tilley,* and Michael Grätzel*

Recent research on photoanodes for photoelectrochemical water splitting has introduced the concept of under- and overlayers for the activation of ultrathin hematite films. Their effects on the photocatalytic behavior were clearly shown; however, the mechanism is thus far not fully understood. Herein, the contribution of each layer is analyzed by means of electrochemical impedance spectroscopy, with the aim of obtaining a general understanding of surface and interface modifications and their influence on the hematite photoanode performance. This study shows that doping of the hematite from the underlayer and surface passivation from annealing treatments and an overlayer are key parameters to consider for the design of more efficient iron oxide electrodes. Understanding the contribution of these layers, a new design for ultrathin hematite films employing a combination of a gallium oxide overlayer with thin niobium oxide and silicon oxide underlayers is shown to achieve a photocurrent onset potential for the photoelectrochemical oxidation of water more negative than 750 mV versus the reversible hydrogen electrode (RHE) at pH 13.6, utilizing Co-Pi as a water oxidation catalyst. It is demonstrated that multilayer hematite thin film photoanodes are a strategy to reduce the overpotential for this material, thereby facilitating more efficient tandem cells.

1. Introduction

The direct conversion of solar energy into a carbon-neutral and transportable fuel is one of the challenging goals in sustainable energy research to date. Photoelectrochemical (PEC) water splitting, which uses semiconductor electrodes to split water into molecular hydrogen and oxygen, is a promising strategy towards this end.[1–3] Considering the mandatory criteria of a photoanode material for PEC water splitting–such as a suitable band gap for the absorption of visible light, excellent aqueous stability, natural abundance of the constituent elements, low cost and non-toxicity–hematite (α-Fe_2O_3) is a very attractive candidate. However, for water splitting to occur efficiently with hematite, several processes must be addressed: facilitating majority charge carrier (electron) conduction to the back contact, improving charge transfer of photogenerated holes at the semiconductor-liquid junction (SCLJ), and passivating surface states, which act to diminish the photovoltage delivered by the hematite through surface recombination and/or band edge unpinning.[4,5]

Due to the disaccord between hematite's short hole diffusion length (2–4 nm)[6] and its two orders of magnitude larger absorption length, it is desirable to use films of a few nanometer thickness to allow for the photogenerated holes to reach the SCLJ before recombining with electrons. In order to provide a high surface area for efficient light harvesting even with very thin absorber films, nanostructuring approaches have been applied to either the semiconductor itself[7–10] or to a host scaffold covered by the α-Fe_2O_3 guest absorber.[11–13]

So far, the successful realization of the host-guest approach is hampered by the low photo-activity of thin hematite layers in contact with the supporting electrode surface.[11] Ultrathin hematite films prepared by different techniques like ultrasonic spray pyrolysis (USP), atmospheric pressure chemical vapor deposition (APCVD) and atomic layer deposition (ALD) on a F:SnO_2 (FTO) glass electrode have served as a model system to further investigate the carrier dynamics of hematite in contact with an aqueous electrolyte.[14–18] Particularly, regarding ALD hematite, the importance of surface states governing the charge transfer kinetics for water photo-oxidation has been recognized. A physical model of Fe_2O_3 explicitly including charge transfer through a surface state has successfully explained the mechanism of water photo-oxidation in this system.[17,19] Similar results have been obtained with APCVD hematite.[20,21] This information is essential to investigate and ameliorate the design of interfaces. Previous studies have shown that in the presence of underlayers such as SiO_x,[22] TiO_2 and Nb_2O_5[23] as

L. Steier, Dr. S. D. Tilley, Prof. M. Grätzel
Institut des Sciences et Ingénierie Chimiques
École Polytechnique Fédérale de Lausanne
CH-1015, Lausanne, Switzerland
E-mail: david.tilley@epfl.ch

I. Herraiz-Cardona, Dr. S. Gimenez,
Dr. F. Fabregat-Santiago
Photovoltaics and Optoelectronic Devices Group
Departament de Física
Universitat Jaume I
12071, Castello, Spain
E-mail: sjulia@uji.es

Prof. J. Bisquert
Department of Chemistry
Faculty of Science
King Abdulaziz University
Jeddah, Saudi Arabia

DOI: 10.1002/adfm.201402742

© 2014 WILEY-VCH Verlag GmbH & Co. KGaA, Weinheim

well as SnO_2[24] or Ga_2O_3[25], the photo-activity of thin hematite photoanodes was increased. On the other hand, focusing on the semiconductor/electrolyte interface, catalysts such as Co-Pi[26] and IrO_2[20,27] as well as functional overlayers such as Al_2O_3, Ga_2O_3 and In_2O_3 were shown to succeed in shifting the onset to more negative potentials.[28,29] This improvement in the photocurrent onset potential is a key aspect to enable unassisted water splitting using tandem configurations [30] and therefore it is crucial to understand its nature. The function of overlayers for hematite photoanodes has been extensively debated[26,29,31] and it was recently suggested that the role of these layers lies in the extension of the space charge region by surface state passivation rather than in surface catalysis.[32]

Herein we aim at further elucidating the effect of performance-enhancing underlayers and overlayers by a mechanistic study using electrochemical impedance spectroscopy (EIS) and physical modeling. We focus on thin hematite films employing a SiO_x or an Nb_2O_5 underlayer and a Ga_2O_3 overlayer prepared by methods reported elsewhere[22,23,28] and summarized in the experimental section. It is shown that the combination of the underlayers with a Ga_2O_3 overlayer yields a favorable shift in photocurrent onset potential towards 0.8 V versus the reversible hydrogen electrode (RHE), indicating an increase in the photovoltage that can be extracted from iron oxide for water oxidation. Furthermore, we apply Co-Pi as a water oxidation catalyst to further reduce the overpotential for water oxidation approaching the flat band potential of hematite.

2. Results and Discussion

The physical model employed is conveyed by the equivalent circuit shown in **Figure 1**a and was detailed in previous studies.[17,19] Under illumination, the circuit consists of a capacitance of the bulk hematite, C_{bulk}, in parallel with a resistance related to the rate of trapping holes in surface states, R_{trap}, and a RC unit consisting of a charge transfer resistance from the surface states, $R_{ct,trap}$, in parallel with a capacitance of the surface states, C_{trap}. In all the samples tested in the present study, the photocurrent onset is coincident with the peak of the surface state capacitance and a valley for the charge transfer resistance from this surface state, $R_{ct,trap}$. As an illustrative example, Figure 1c shows the results for an USP Fe_2O_3 sample. This behavior clearly indicates that the hole transfer predominantly happens through a surface state in USP hematite. In the dark, the surface state is not identified and the equivalent circuit employed consists of a simple Randles' circuit (Figure 1b) used for the Mott–Schottky (MS) analysis herein.

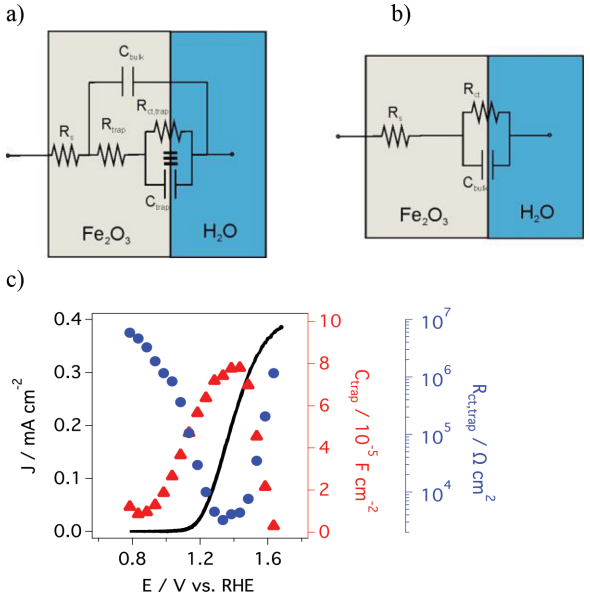

Figure 1. Physical equivalent circuit model employed a) under illumination and b) in the dark for photoelectrochemical water splitting with hematite. (c) Representative plot of a USP Fe_2O_3 photoanode showing that the photocurrent onset is coincident with the C_{trap} peak and the $R_{ct,trap}$ valley. This behavior has been systematically observed for all the samples analyzed in the present study.

We first focus on the electrochemical contribution of the SiO_x or the Nb_2O_5 underlayers to the activation of hematite photoanodes before elucidating the nature of the Ga_2O_3 overlayer. **Figure 2** shows typical current density–voltage (J–V) curves and their corresponding MS plots of as prepared (a-b) and air-annealed (c-d) thin hematite films employing Nb_2O_5, SiO_x or no underlayer. Due to space charge layer limitations, these samples were chosen to be thicker for EIS measurements (approximately 30 nm) and therefore the enhancement of photoactivity due to the employed underlayer compared to ultrathin hematite films (where these underlayers revive the photoelectrical performance of the photoanodes) is less dramatic.[22,23] The photocurrent plateau is remarkably higher for the underlayer treated hematite samples and has been attributed to a change in film morphology in the case of a SiO_x underlayer[22] and to a hole blocking effect in the case of the Nb_2O_5 underlayer.[23] In addition to these observations, here we find a doping contribution from these underlayers (obtained from MS analysis). From the MS plots the charge carrier density, N_D, can be extracted and is inversely proportional to the slope (Equation (1)).

$$\left(\frac{A_S}{C_{bulk}}\right)^2 = \frac{2}{q\varepsilon\varepsilon_0 N_D}\left(V - E_{FB} - \frac{k_B T}{q}\right) \quad (1)$$

With $\left(\frac{C_{bulk}}{A_S}\right)$ being the surface area corrected space charge capacitance, V the applied potential, E_{FB} the flat-band potential of the semiconductor, $k_B = 1.38 \cdot 10^{-23}\,\mathrm{J K^{-1}}$, T = 298 K, $q = 1.602 \cdot 10^{-19}\,\mathrm{C}, \varepsilon_0 = 8.85 \cdot 10^{-12}\,\mathrm{C^2 J^{-1} m^{-1}}$ and $\varepsilon = 32$ for hematite.[19,33]

Representative results of the MS analysis based on at least 3 samples of each kind are summarized in **Table 1**. However, it is already directly visible from the slope of the MS plots shown in Figure 2b that the SiO_x and the Nb_2O_5 layers have a higher charge carrier density and serve as doping agents for hematite according to the following proposed defect mechanisms:

$$Nb_2O_5 \xrightarrow{Fe_2O_3} 2Nb_{Fe} + 3O_O + O_2 \quad (2)$$

$$Nb_{Fe} \rightleftharpoons Nb_{Fe}^{\cdot\cdot} + 2e'_{cb} \quad (3)$$

© 2014 WILEY-VCH Verlag GmbH & Co. KGaA, Weinheim

DOI: 10.1002/adfm.201402742

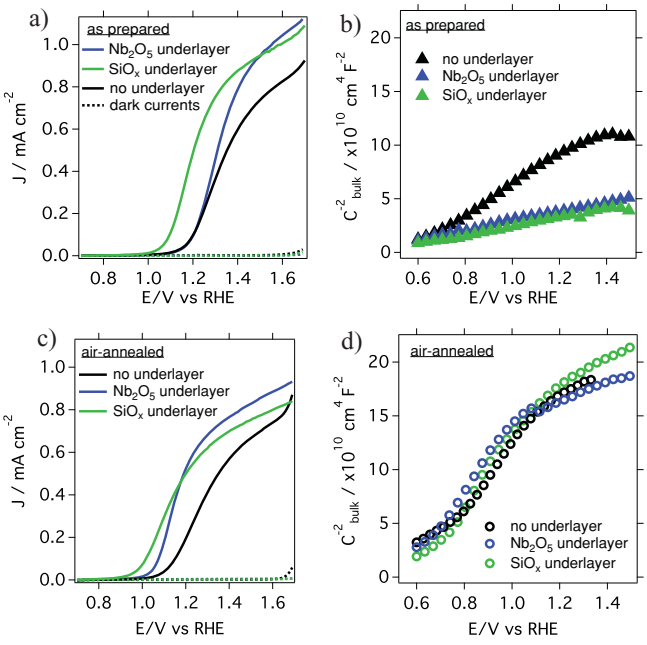

Figure 2. Current Density–Voltage curves (left) and Mott–Schottky measurements (right) of hematite photoanodes employing an Nb_2O_5 (blue), a SiO_x (green) or no underlayer (black) compared in an "as prepared" state (a-b) and after 2 h of annealing in air at 500 °C (c-d). J–V measurements were obtained in the dark (dashed lines) and under AM 1.5G simulated solar illumination (100 mWcm^{-2}, solid lines). The corresponding MS measurements were carried out in the dark. The electrolyte was 1 M NaOH (pH 13.6).

$$2SiO_2 \xrightarrow{Fe_2O_3} 2Si_{Fe} + 3O_O + \frac{1}{2}O_2 \quad (4)$$

$$Si_{Fe} \rightleftharpoons Si_{Fe}^{\cdot\cdot} + e'_{cb} \quad (5)$$

Charge carrier concentrations increase by a factor of 2 when an underlayer is present ($N_D \approx 7 \cdot 10^{19}$ cm^{-3}). Ultrathin hematite films (approximately 10–15 nm) employing these underlayers also measured in the context of this work even show a three times higher donor density ($N_D \approx 2 \cdot 10^{20}$ cm^{-3}), which can be attributed to gradient doping from the underlayer with a stronger doped region near the underlayer. XPS measurements confirmed the presence of the dopant atoms at the hematite surface in thicker (>30 nm) samples, where the underlying substrate is not seen (Figure S1 in SI). The increase in electron density in doped hematite films is correlated with an increase in the photocurrent plateaus (Figure 2a). The calculated space charge layer width, W_{SC}, is several nanometers shorter for the Nb- and Si-doped samples than for the samples without an underlayer (Figure S2 in SI). Thus, the higher photocurrents can be explained by a stronger band bending in the surface region of the film, and therefore improved charge separation in the space charge layer, which leads to reduced recombination at the hematite surface.

The contribution of the doping effect is especially visible in ultrathin hematite photoanodes while the influence on film morphology and/or surface state passivation[34] becomes predominant in thicker hematite films if the doping level is sufficiently high to allow for high conductivity. **Figure 3**a shows the influence of the Nb_2O_5 underlayer compared to Al_2O_3 and Ga_2O_3 underlayers (all underlayers 2 nm thick) on the J–V performance of approximately 10 nm hematite photoanodes. It is observed that the underlayers with a 3-valent cation (Al^{3+} and Ga^{3+}) improve slightly the photocurrent of the completely inactive hematite anode (black) most likely due to their influence on the uniformity of the grown hematite film. However, Nb_2O_5 clearly revives the hematite electrode of the same thickness (Absorptance measurements, see Figure S3 in the SI) due to its doping effect. It cannot be excluded that Nb_2O_5 also has a morphological influence on the hematite film formation, though it is not the predominant effect in thin films. It is likely that the "dead-layer-effect" is overcome for Nb_2O_5 due to the introduction of band bending in the ultrathin (10 nm) hematite layer (Equation S3 in SI). For thicker hematite films of approximately 30 nm thickness, which exceed the thickness where the so-called "dead layer effect" is seen, the Ga_2O_3 underlayer shows a more negative onset potential than the Nb_2O_5 underlayer while maintaining the same photocurrent plateau (Figure 3b). This phenomenon points to a surface state passivation effect that is dominating the onset potential,[34] and is consistent with

Table 1. Representative results for flatband potential, E_{FB}, charge carrier concentration, N_D, and space charge width, W_{SC} (at 1.23 V), from Mott–Schottky measurements in the dark. Sample thicknesses varied between approximately 19 nm or 30 nm but W_{SC} did not exceed film thickness.

		no underlayer	Nb_2O_5 underlayer	SiO_x underlayer
as prepared	E_{FB}/V vs RHE	0.60	0.45	0.46
	$N_D/10^{19}$ cm^{-3}	3.00	6.53	7.27
	W_{SC}/nm	8.63	6.50	6.14
air-annealed	E_{FB}/V vs RHE	0.51	0.54	0.60
	$N_D/10^{19}$ cm^{-3}	1.31	1.27	1.22
	W_{SC}/nm	13.9	13.8	13.6
Ar-annealed	E_{FB}/V vs RHE	0.25	0.32	
	$N_D/10^{19}$ cm^{-3}	4.50	8.70	
	W_{SC}/nm	8.78	6.08	

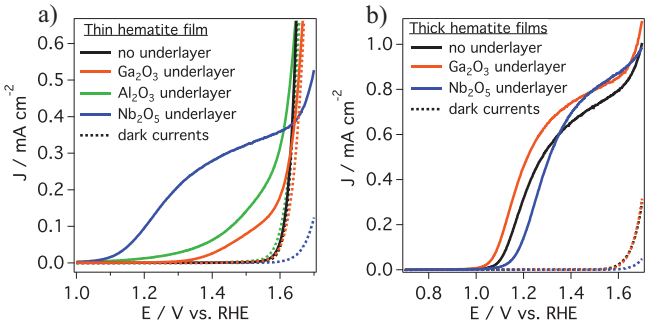

Figure 3. Influence of Ga_2O_3 (orange), Al_2O_3 (green) and Nb_2O_5 (blue) underlayer treatment on the J–V performance of a) ultrathin hematite anodes (approximately 10 nm) and b) thicker hematite anodes (approximately 30 nm). J–V measurements were obtained in the dark (dashed lines) and under AM 1.5G simulated solar illumination (100 mWcm^{-2}, solid lines). The electrolyte was 1M NaOH (pH 13.6).

© 2014 WILEY-VCH Verlag GmbH & Co. KGaA, Weinheim

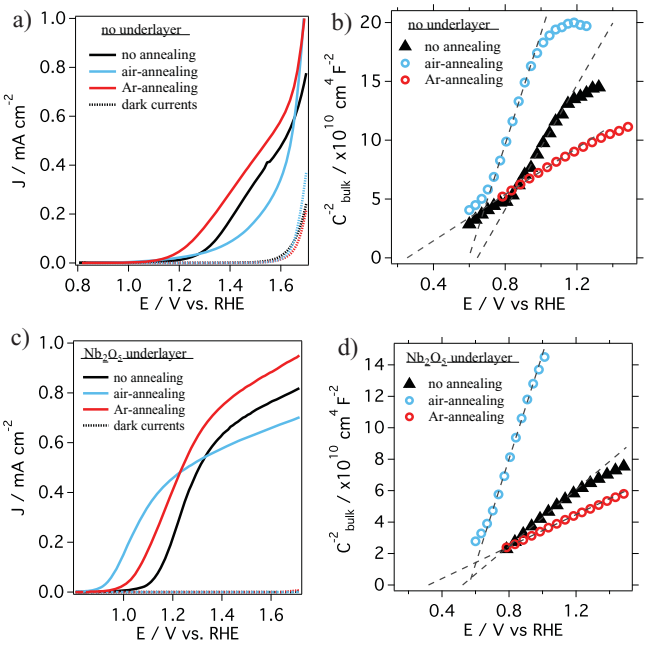

Figure 4. J–V curves (left) and MS measurements (right) of thin hematite photoanodes employing a–b) no underlayer or c–d) a 2 nm Nb_2O_5 underlayer measured after annealing in air (light blue) or in argon (red) and compared to the as prepared samples (black) of approximately 19 nm thick. Photocurrent was measured under AM 1.5G simulated solar illumination (100 mWcm^{-2}). Dark current measurements are shown in dashed lines ((a) and (c)). MS measurements were carried out in the dark. The electrolyte was 1 M NaOH (pH 13.6).

the results obtained in Figure 2c where the Nb_2O_5 treated film improves its photocurrent onset potential after air-annealing, but suffers from a decreased photocurrent plateau due to a decreased conductivity (Figure 2d). The same effect is observed for the SiO_x underlayer (compare Figure 2a and c). The effect of annealing on surface state passivation is further analyzed in the context of our Ga_2O_3 overlayer.

The extracted charge carrier density from the MS plots takes both doping effects into account: the n-doping from the oxide underlayers (when present) as well as the n-doping of hematite by oxygen vacancies. The latter's influence on the doping level is visible in annealing experiments performed in air (bottom part of Figure 2). Figure 2d shows that all three samples suffer from a severe decrease in doping density and equilibrate around practically the same value of $N_D \approx 1.3 \cdot 10^{19}$ cm^{-3}. Again, the decrease in charge carrier density and the increase in the space charge layer width correlate with a lower plateau current (200 μA cm^{-2} decrease for the samples employing an underlayer and 100 μA cm^{-2} decrease for the standard hematite, Figure 2c). We hypothesized that the decrease in charge carrier concentration was due to filling of oxygen vacancies by oxygen during the air-annealing process. We therefore carried out annealing experiments under argon atmosphere. Indeed, the data shown in **Figure 4** demonstrate oxygen-dependent photoanode behavior. In contrast to the air-annealed hematite samples where the charge carrier concentration and photocurrent plateau are decreased, annealing in argon atmosphere results in a higher carrier concentration as seen in the MS plots for samples both with and without extrinsic doping from an underlayer (Figure 4d and (b) respectively).

In the case of a hematite film without any foreign dopant, this behavior can be explained by the defect equilibrium formed by oxygen vacancies, $(V_O^{\cdot\cdot})$ Equation (6). The degree of doping by oxygen vacancies in hematite is known to be dependent on oxygen partial pressure according to $n_C \propto p_{O_2}^{-\frac{1}{6}}$ resulting from applying the mass action law on the following equilibrium equation:

$$\frac{1}{2}O_2 + V_O^{\cdot\cdot} + 2e' \overset{Fe_2O_3}{\Longleftrightarrow} O_O \quad (6)$$

The annealing in argon therefore forms additional oxygen vacancies due to the reduced oxygen partial pressure, while annealing in air fills the vacancies that are normally present. Comparing the resulting J–V curves with the results obtained from MS analysis, the same correlation is observed in the sense that the higher doped film in the case of argon annealing shows a higher photocurrent plateau compared to the non-annealed and air-annealed samples. However, it seems that the oxygen vacancies are a mixed blessing in the sense that they increase the plateau current but increase the voltage onset for photo-oxidation of water as well.

In the case of Nb- or Si-doped hematite the defect equilibrium during annealing in air involves formation of cation vacancies according to Equation (7):

$$\frac{1}{2}O_2 + 2e' \overset{Fe_2O_3}{\Longleftrightarrow} O_O + \frac{2}{3}V_{Fe}^{'''} \quad (7)$$

During the annealing process in air, oxygen can be incorporated as O^{2-} in the hematite lattice (O_O). The excess oxygen in the lattice created in this manner is then compensated by cation vacancies, $\left(V_{Fe}^{'''}\right)$, according to Equation (7). Cation vacancies are surrounded by anions and therefore are strong recombination centers for holes resulting in lower photocurrents in the J–V measurements (Figure 4a). In the case of annealing in oxygen-free atmosphere at temperatures that allow ion mobility, the hematite film is further doped from the underlayer, as this doping is sensitive to the oxygen partial pressure (Equations (2)–(5)). Hence, the increase in charge carrier concentration after annealing in argon atmosphere (red circles in Figure 4d) is resulting from additional electronic doping from the underlayer. These results show the tunable intrinsic doping level of hematite to be kept in mind for the preparation of standardized hematite thin films prepared by different deposition techniques.

In the following we focus on further improving the photocurrent onset potential, and we chose Ga_2O_3 as an abundant material previously reported to give a remarkable shift towards more negative potentials.[28] We deposited Ga_2O_3 as an overlayer onto the annealed samples by chemical bath deposition (CBD) followed by annealing in air (as post-annealing in argon deteriorated the anode performance). The morphology of the deposited Ga_2O_3 structure is shown in **Figure 5** (a-b). It shows Ga_2O_3 trunk formation with trunks on the order of 150–300 nm depending on the time of the CBD. Since Ga_2O_3 does not form a conformal layer on top of the hematite film, the surface of

© 2014 WILEY-VCH Verlag GmbH & Co. KGaA, Weinheim
Adv. Funct. Mater. **2014**,
DOI: 10.1002/adfm.201402742

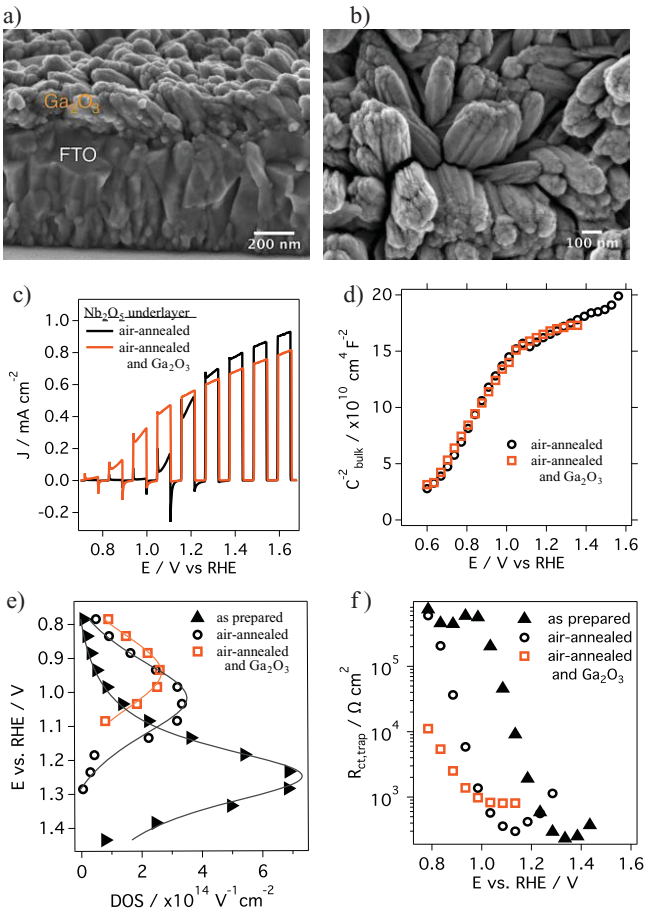

Figure 5. Characteristics of hematite photoanodes upon addition of a Ga_2O_3 overlayer on a Nb-doped hematite photoanode. Shown are a) cross-sectional and b) top-view SEM images of the Ga_2O_3 structure on a (barely visible) ultrathin (approximately 16 nm) hematite layer deposited on FTO glass. c) Light chopping experiments of air-annealed Nb-doped thin (approximately 30 nm) hematite photoanodes before (black) and after Ga_2O_3 CBD (orange). d) MS plots of the samples shown in c) measured in the dark. e) Applied potential versus density of surface states (DOS) extracted from C_{trap}. Shown are air-annealed samples from c) before (black hollow circles) and after Ga_2O_3 deposition (orange hollow squares). In addition, a non-annealed sample is shown for comparison (black filled triangles). A Lorentzian fit for each sample guides the eye but also indicates the shift in maximum of the DOS at a certain potential. f) Charge transfer resistances from surface states, $R_{ct,trap}$, versus applied potential for samples from e) show a minimized resistance in presence of a Ga_2O_3 overlayer. Measurements shown in (c), (e) and (f) were carried out with simulated AM 1.5G (100 mWcm^{-2}) light. The electrolyte was 1 M NaOH (pH 13.6).

hematite is assumed to be exposed to the solution. It should be noted that the relatively thick Ga_2O_3 structure as shown herein does not filter the visible light as the J–V curves from both front and backside illumination overlap one another (Figure S3 in SI).

Figure 5c shows two important results obtained for an electrode design employing both an Nb_2O_5 underlayer as well as a Ga_2O_3 overlayer. First, upon addition of the Ga_2O_3 overlayer the photocurrent onset potential is shifted by 200 mV, reaching 0.8 V vs RHE. This onset potential has thus far only been obtained by using a catalyst[35] or by employing alternative structures such as buried p-n homo-[18] or hetero-junction hematite photoanodes[16] or using temperatures as high as 800 °C.[34] Second, light-chopping experiments performed with these photoanodes show that Ga_2O_3 remarkably suppresses transient peaks especially in the photocurrent onset region. The reduction of the photocurrent transients means that either Ga_2O_3 is behaving as a water oxidation catalyst with improved charge-transfer properties relative to hematite, or it is passivating surface states. Although we thought any catalytic effect unlikely, we deposited Ga_2O_3 directly onto FTO glass, omitting the hematite layer. The results shown in Figure S4 confirm that neither catalytic nor photocatalytic effects were observed for Ga_2O_3 deposited on F:SnO_2 (Tec15) glass.

In parallel, the assumption of surface passivation was investigated. Figure 5e shows the density of surface states (DOS) at a given potential measured under illumination. The DOS was extracted from the trap capacitance, C_{trap}, using Equation (8)

$$C_{trap} = q \cdot DOS \tag{8}$$

where C_{trap} was extracted from the equivalent circuit presented in Figure 1a. More details about the calculation of C_{trap} are provided in the SI.[36] From the density of surface states representation it is shown that surface passivation is evident for air-annealed samples (black hollow circles) and then further passivation is observed in the presence of a Ga_2O_3 overlayer (orange hollow squares). Interestingly, the potential position of the DOS peaks changes (along with the photocurrent onset) from 1.25 V_{RHE} for the fresh sample to 1.02 V for the air-annealed sample and 0.94 V in the case of a Ga_2O_3 overlayer after annealing.

The shift of the DOS maxima in Figure 5e after air-annealing (black triangles compared to black hollow circles) coincides with the approximately 200 mV photocurrent onset potential shift observed in Figure 4c (light blue compared to black line). This relation is illustrated in **Figure 6**. The onset of photocurrent occurs as soon as half of the surface states are emptied, therefore decreasing surface recombination of the trapped electrons with holes from the valence band. Surface states located energetically higher, allow for an earlier photocurrent onset potential as they are emptied at less applied bias. The change in density and energetic position of these states is most likely due to the decrease in oxygen vacancies at the surface during annealing in ambient air as is confirmed by our MS experiments (Figure 4).

With a Ga_2O_3 overlayer, a subsequent surface state passivation (orange squares in Figure 5e) as well as an additional 200 mV shift in photocurrent onset towards more negative potentials (Figure 5c) is observed. Again, part of this shift can be correlated with the shift of the energetic position of the DOS maxima of approximately 100 mV after Ga_2O_3 deposition. This behavior is also correlated to the shift of the minimum of the charge transfer resistance ($R_{ct,trap}$) as shown in Figure 5f, clearly indicating that the trap state is dominating the hole transfer kinetics for water oxidation, and that the effect of the Ga_2O_3 overlayer is affecting the energetic distribution of the trap state. From our MS measurements (Figure 5d), the shifts reported in Figure 5e and (f) could not be ascribed to a shift of the flatband potential of hematite in good agreement with previous studies.[32] Furthermore, Ga_2O_3 was deposited by ALD on

© 2014 WILEY-VCH Verlag GmbH & Co. KGaA, Weinheim

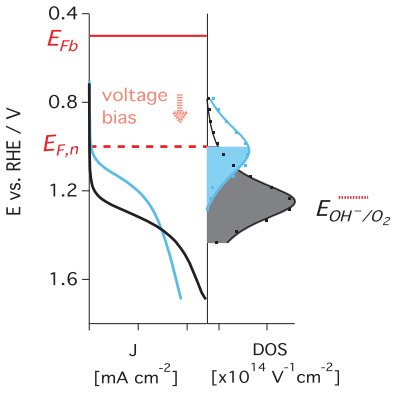

Figure 6. Energetic alignment of the density of surface states (DOS) and the photocurrent curves (J) for Nb-doped hematite photoanodes before (black) and after air-annealing (light blue). The data is taken from Figure 4c and 5e for direct comparison. Also indicated is the measured flatband potential, E_{Fb}, and the quasi-Fermi level of electrons, $E_{F,n}$, under illumination.

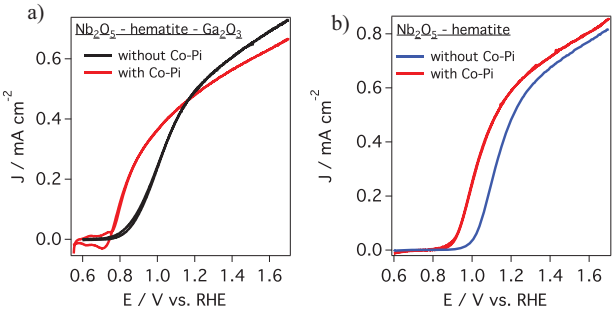

Figure 7. Photocurrent measurements of Nb-doped hematite thin films a) employing a CBD grown Ga_2O_3 overlayer with (red) and without (black) Co-Pi photo-electrodeposited catalyst and compared to b) the control Nb-doped hematite electrode annealed in air at 500 °C without the Ga_2O_3 overlayer before (blue) and after (red) Co-Pi photo-electrodeposition. Cyclovoltammetric scans were carried out with simulated AM 1.5G (100 mWcm^{-2}) light with a scan rate of 1 mV/s and were illuminated from the FTO side. The electrolyte was 1 M NaOH (pH 13.6).

the hematite film and it was interesting that only thicker films of Ga_2O_3 showed a slight shift in the onset potential after air-annealing at 550 °C for 1 h, though still not reaching the onset shift of the Ga_2O_3 deposited by CBD (Figure S6 in SI). Omitting the annealing treatment, the electrodes with the Ga_2O_3 overlayer deposited either by ALD or CBD showed resistive J–V behavior (data not shown). This observation supports our hypothesis that the hematite surface must be exposed to the solution and that the annealing process is mandatory to form cracks in the ALD as well as in the CBD grown Ga_2O_3 overlayer, and that suppression of the back reaction at the SCLJ is not the predominant mechanism of the CBD-Ga_2O_3 overlayer (as opposed to what was reported for Al_2O_3[29] and SnO_2[37] on hematite nanoparticles). The surface state passivation could result from a decreased oxygen vacancy concentration at the hematite surface by the Ga_2O_3 overlayer that is less prone to oxygen vacancy formation than Fe_2O_3 itself.

Finally, we sought to further improve the photocurrent onset potential through the addition of a water oxidation catalyst to our multilayer hematite photoanodes. As the hematite surface was only accessible through cracks in the Ga_2O_3 overlayer, photoelectrodeposition was the most efficient technique to deposit the catalyst (spin-coating of catalysts, for example, was unsuccessful). Thus, we photoelectrodeposited Co-Pi onto the Nb-doped hematite photoanode (with Ga_2O_3 overlayer) and could indeed obtain an additional 100 mV shift in the onset potential to more negative than 0.75 V vs RHE (**Figure 7**). Co-Pi photo-electrodeposition on a control Nb-doped hematite electrode without our Ga_2O_3 overlayer showed a 150 mV more positive photocurrent onset potential which is in agreement with the literature.[26] With this result, we have substantially lowered the overpotential for water oxidation with these photoanodes, and a mere 200 mV of bias is required (versus the flatband potential) for the onset of photocurrent (E_{FB} = 0.54 V vs RHE for air-annealed Nb-doped thin hematite films (Table 1)).

3. Conclusions

Using impedance spectroscopy analysis and physical modeling, it was shown that doping from underlayers into hematite thin films prepared by ultrasonic spray pyrolysis plays an important role in their performance, in addition to the influence of the underlayers on film growth and suppression of electron-hole recombination at the FTO/SC interface reported before. Both the Nb_2O_5 and the SiO_x underlayers that were investigated herein show an increase in n-doping in the hematite film. The increase in electron density is correlated with an increase in the photocurrent plateaus of the doped films, which is attributed to a stronger electric field in the surface region due to stronger band bending in the thinner space charge layer and therefore better charge separation and reduced recombination at the hematite/solution interface.

Furthermore, it was shown that hematite, which tends to be n-doped by oxygen vacancies, is sensitive to the annealing environment. Oxygen present in the atmosphere tends to fill oxygen vacancies during the annealing process leading to a decrease in the photocurrent plateau. It was shown that annealing in oxygen-free atmosphere increases the carrier concentration in the film most probably due to subsequent doping from the underlayer and hence increases the photocurrent plateau. Additionally, annealing Nb-doped hematite films to 500 °C or 550 °C in air shifts the photocurrent onset potential negative, which was attributed to surface state passivation.

Finally, we have shed light on the nature of the favorable photocurrent onset potential shift in the presence of a Ga_2O_3 overlayer. There seem to be two causes for this 200 mV shift. First, the energetic position of the trap states shifts 100 mV negatively, which can partially explain the observed potential shift. Second, the absolute value of the density of surface states peak together with the photocurrent transient experiments clearly indicate that passivation of surface states takes place, enabling a greater photovoltage to be extracted from the iron oxide.

In summary, this study elucidates that there are at least two major concepts to improve the catalytic performance of thin hematite films for photo-electrochemical water splitting. Firstly, the conductivity of hematite and band bending dominate the increase in the photocurrent plateau, while the photocurrent onset potential is dominated by surface state passivation (**Figure 8**).

© 2014 WILEY-VCH Verlag GmbH & Co. KGaA, Weinheim

DOI: 10.1002/adfm.201402742

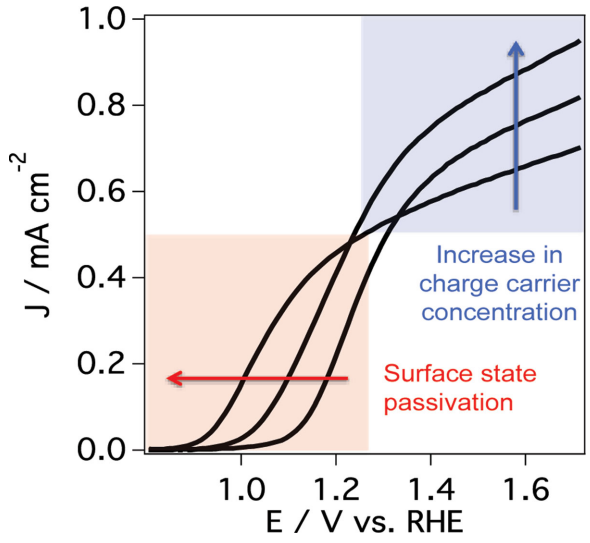

Figure 8. Illustration of the mechanisms dominating the photocurrent plateau (blue) and the photocurrent onset potential (red) in a J–V curve of thin hematite film photoanodes for photoelectrochemical water splitting.

In the end, a new hematite thin film photoanode design employing Nb_2O_5 and/or SiO_x underlayers combined with the Ga_2O_3 overlayer was developed reaching an onset potential of 0.8 V vs RHE without any water oxidation catalyst, and more negative than 0.75 V vs RHE with Co-Pi as a catalyst, while maintaining a high photocurrent plateau and using cheap, abundant and non-toxic materials.

4. Experimental Section

All samples were prepared on high temperature resistant alumino-borosilicate glass coated with fluorine-doped tin oxide (FTO) serving as a transparent conducting oxide (10 × 10 cm, 10 Ω, Solaronix, cut into 1.25 cm × 3.4 cm substrates). The substrates were cleaned by successive ultra-sonication for 15 min with acetone, soap, water and 2-propanol as previously reported.[22] A 2 nm thick niobium oxide layer was deposited on the FTO by atomic layer deposition using a Savannah 100 instrument (Cambridge Nanotechnology). (tert-butylimido)tris(diethylamino) niobium (TBTDEN, Digital Specialty Chemicals, 99.8%) and bidistilled water (AppliChem) were pulsed into a nitrogen flow (20 sccm, Carbagas, 99.9999% purity) at 150 °C with exposure times of 10 s, resulting in a growth rate of 0.56 Å/cycle, estimated from ellipsometry measurements on a Si-wafer. A silicon oxide underlayer was deposited at a surface temperature of 370 °C by spray pyrolysis (2 ml/sample of a 10 Vol% tetraethoxysilane (99.999%, Aldrich) solution in ethanol (99.9%, Fluka)). Ga_2O_3 and Al_2O_3 underlayers of 2 nm in thickness were deposited on the FTO by atomic layer deposition using a Savannah 100 instrument (Cambridge Nanotechnology). Tris(dimethylamido)gallium(III) (98%, Aldrich) for Ga_2O_3 or trimethylaluminium (TMA, 94%, ABCR) for Al_2O_3 and bidistilled water (AppliChem) were pulsed alternatingly into a nitrogen flow (10 sccm, Carbagas, 99.9999% purity) and exposed for 30 s to the FTO heated to 150 °C. The growth rate of the Ga_2O_3 layer was estimated to be 1 Å/cycle on a Si-wafer by ellipsometry. The growth rate of the Al_2O_3 layer was estimated to be 1.7 Å/cycle on a Si-wafer.

Iron oxide was deposited on cleaned FTO (or FTO coated by the underlayer) by ultrasonic spray pyrolysis (USP) at a surface temperature of 415 °C (10 mM $Fe(acac)_3$ (99.9%) solution; 1 ml every 30 s, 12 ml/min). Air-annealed or argon-annealed samples were heated in air or argon to 500 °C for 2 h with a heating and cooling rate of 10 °C/min. A gallium oxide layer was deposited by chemical bath deposition (CBD) (10 mM $Ga(NO_3)_3 \times x\ H_2O$ (x = 6, 9), 1 M Urea, 78 – 83 °C). 15 minutes after Urea addition the samples were rinsed with distilled water and annealed in air at 550 °C for 1 h together with their control samples (without Ga_2O_3). Co-Pi was photo-electrodeposited under AM 1.5G simulated sunlight at 0.4 V vs Ag/AgCl, KCl (sat'd) for 1000 s in a Co^{2+} enriched phosphate buffer solution (0.5 mM $Co(NO_3)_2 \times 6\ H_2O$ in 0.1 M potassium phosphate buffer, pH 7).

Photocurrent measurements were performed in 1 M NaOH aqueous solution (pH 13.6) using a three-electrode configuration, with a Pt wire counter electrode and an Ag/AgCl, KCl (sat'd) reference electrode. Simulated sunlight was generated from a 450 W xenon lamp (Osram, ozone free) passed through a KG3 filter (3 mm, Schott) with a measured intensity equivalent to standard AM 1.5G sunlight (100 $mWcm^{-2}$, spectrally corrected) at the sample face masked to 0.5 cm^2. Without a catalyst, the potential was swept anodically at a scan rate of 20 mV s^{-1} (after it was proven that the sweeps did not differ from scans at lower scan rates). In the presence of Co-Pi, cyclovoltammogramms were taken at a scan rate of 1 mV/s. Higher scan rates showed capacitive behavior (and a more cathodic potential onset due to the capacitive current).

Mott-Schottky measurements were carried out in the dark with the same three-electrode cell in 1 M NaOH solution. Full impedance spectra were measured with a SP-300 (BioLogic Science Instruments) at frequencies from 1 MHz to 0.1 Hz with a sinusoidal potential perturbation of 25 mV. The range of the bias potential was equal to that of the photocurrent measurements (0.6 – 1.7 V vs RHE). The capacitance was extracted from the fitting according to the standard Randles circuit fitted with Zview (Scribner Associates).

Impedance spectra under illumination were acquired with a FRA equipped PGSTAT-30 potentiostat from Autolab. The electrodes were illuminated using a 300 W Xe lamp, where the light intensity was adjusted with a thermopile to 100 mW cm^{-2}. EIS measurements were carried out by applying a 20 mV AC signal and scanning in a frequency range between 100 kHz and 50 mHz, at different applied bias. All potentials have been referenced to the reversible hydrogen electrode (RHE) by the expression:

$$V_{RHE} = V_{Ag/AgCl} + 0.210V + 0.059V \cdot pH \quad (9)$$

X-ray photoelectron spectroscopy (XPS) data were collected by Axis Ultra (Kratos analytical, Manchester, UK) under ultra-high vacuum condition (<10^{-8} Torr), using a monochromatic Al K_α X-ray source (1486.6 eV), in the laboratory of Chemical Metallurgy at EPFL. The source power was maintained at 150 W (10 mA, 15 kV). The emitted photoelectrons were sampled from a square area of 750 × 350 μm. Gold (Au $4f_{7/2}$) and copper (Cu $2p_{3/2}$) lines at 84.0 eV and 932.6 eV, respectively, were used for calibration, and the adventitious carbon 1s peak at 285 eV as an internal standard to compensate for any charging effects.

Scanning electron microscopy secondary electron images were acquired with a Merlin microscope (Zeiss).

Supporting Information

Supporting Information is available from Wiley Online Library or from the author.

Acknowledgements

L.S., S.D.T. and M.G. thank the Swiss Federal Office for Energy (PECHouse Competence Center, contract number SI/500090–02) for financial support. SG and F.F-S acknowledge financial support from Jaume I University through research project P1·1B2011–50. MG thanks the European Research Council (ERC) for financial support of this

© 2014 WILEY-VCH Verlag GmbH & Co. KGaA, Weinheim

work under the Advanced Research Grant no. 247404 MESOLIGHT. We thank Prof. Kevin Sivula for fruitful discussions as well as Nicolas Xanthopolous for the XPS measurements.

Received: August 11, 2014
Published online:

[1] P. J. Boddy, *J. Electrochem. Soc.*, **1968**, *115*, 199-&.
[2] A. Fujishima, K. Honda, *Nature* **1972**, *238*, 37-+.
[3] B. A. Pinaud, J. D. Benck, L. C. Seitz, A. J. Forman, Z. Chen, T. G. Deutsch, B. D. James, K. N. Baum, G. N. Baum, S. Ardo, H. Wang, E. Miller, T. F. Jaramillo, *Energy Environ. Sci.* **2013**, *6*, 1983–2002.
[4] K. Sivula, F. Le Formal, M. Gratzel, *ChemSusChem* **2011**, *4*, 432–449.
[5] A. Duret, M. Gratzel, *J. Phys. Chem. B* **2005**, *109*, 17184–17191.
[6] J. H. Kennedy, K. W. Frese, *J. Electrochem. Soc.* **1978**, *125*, 709–714.
[7] J. Brillet, M. Gratzel, K. Sivula, *Nano Lett* **2010**, *10*, 4155–4160.
[8] K. Sivula, J. Brillet, M. Gratzel, *Proc. SPIE 7770, Solar Hydrogen and Nanotechnology V* **2010**, *77700G*, 1–6 doi:10.1117/12.860199.
[9] K. Sivula, R. Zboril, F. Le Formal, R. Robert, A. Weidenkaff, J. Tucek, J. Frydrych, M. Gratzel, *J. Am. Chem. Soc.* **2010**, *132*, 7436–7444.
[10] L. Li, Y. Yu, F. Meng, Y. Tan, R. J. Hamers, S. Jin, *Nano Lett.* **2012**, *12*, 724–731.
[11] K. Sivula, F. Le Formal, M. Gratzel, *Chem. Mater.* **2009**, *21*, 2862–2867.
[12] M. Stefik, M. Cornuz, N. Mathews, T. Hisatomi, S. Mhaisalkar, M. Gratzel, *Nano Lett.* **2012**, *12*, 5431–5435.
[13] Y. J. Lin, S. Zhou, S. W. Sheehan, D. W. Wang, *J. Am. Chem. Soc.* **2011**, *133*, 2398–2401.
[14] S. R. Pendlebury, M. Barroso, A. J. Cowan, K. Sivula, J. Tang, M. Grätzel, D. Klug, J. R. Durrant, *Chem. Commun.* **2011**, *47*, 716.
[15] A. J. Cowan, C. J. Barnett, S. R. Pendlebury, M. Barroso, K. Sivula, M. Grätzel, J. R. Durrant, D. R. Klug, *J. Am. Chem. Soc.* **2011**, *133*, 10134–10140.
[16] M. T. Mayer, Y. J. Lin, G. B. Yuan, D. W. Wang, *Accounts Chem. Res.* **2013**, *46*, 1558–1566.
[17] B. Klahr, S. Gimenez, F. Fabregat-Santiago, J. Bisquert, T. W. Hamann, *Energy Environ. Sci.* **2012**, *5*, 7626–7636.
[18] Y. Lin, Y. Xu, M. T. Mayer, Z. I. Simpson, G. McMahon, S. Zhou, D. Wang, *J. Am. Chem. Soc.* **2012**, *134*, 5508–5511.
[19] B. Klahr, S. Gimenez, F. Fabregat-Santiago, T. Hamann, J. Bisquert, *J. Am. Chem. Soc.* **2012**, *134*, 4294–4302.
[20] L. Badia-Bou, E. Mas-Marza, P. Rodenas, E. M. Barea, F. Fabregat-Santiago, S. Gimenez, E. Peris, J. Bisquert, *J. Phys. Chem. C* **2013**, *117*, 3826–3833.
[21] A. Braun, K. Sivula, D. K. Bora, J. F. Zhu, L. Zhang, M. Gratzel, J. H. Guo, E. C. Constable, *J. Phys. Chem. C* **2012**, *116*, 16870–16875.
[22] F. Le Formal, M. Grätzel, K. Sivula, *Adv. Funct. Mater.* **2010**, *20*, 1099–1107.
[23] T. Hisatomi, H. Dotan, M. Stefik, K. Sivula, A. Rothschild, M. Gratzel, N. Mathews, *Adv. Mater* **2012**, *24*, 2699–2702.
[24] Y. Q. Liang, C. S. Enache, R. van de Krol, *Int. J. Photoenergy* **2008**, doi: 10.1155/2008/739864.
[25] T. Hisatomi, J. Brillet, M. Cornuz, F. Le Formal, N. Tétreault, K. Sivula, M. Grätzel, *Faraday Discussions* **2012**, *155*, 223–232.
[26] B. Klahr, S. Gimenez, F. Fabregat-Santiago, J. Bisquert, T. W. Hamann, *J. Am. Chem. Soc.* **2012**, *134*, 16693–16700.
[27] S. D. Tilley, M. Cornuz, K. Sivula, M. Grätzel, *Angew. Chem. Int. Ed.* **2010**, *49*, 6405–6408.
[28] T. Hisatomi, F. Le Formal, M. Cornuz, J. Brillet, N. Tétreault, K. Sivula, M. Grätzel, *Energy Environ. Sci.* **2011**, *4*, 2512.
[29] F. Le Formal, N. Tétreault, M. Cornuz, T. Moehl, M. Grätzel, K. Sivula, *Chem. Sci.* **2011**, *2*, 737.
[30] J. Brillet, M. Cornuz, F. Le Formal, J. H. Yum, M. Gratzel, K. Sivula, *J. Mater. Res.* **2010**, *25*, 17–24.
[31] M. Barroso, A. J. Cowan, S. R. Pendlebury, M. Gratzel, D. R. Klug, J. R. Durrant, *J. Am. Chem. Soc.* **2011**, *133*, 14868–14871.
[32] M. Barroso, C. A. Mesa, S. R. Pendlebury, A. J. Cowan, T. Hisatomi, K. Sivula, M. Gratzel, D. R. Klug, J. R. Durrant, *Proc. Natl. Acad. Sci. USA* **2012**, *109*, 15640.
[33] J. A. Glasscock, P. R. F. Barnes, I. C. Plumb, A. Bendavid, P. J. Martin, *Thin Solid Films* **2008**, *516*, 1716–1724.
[34] O. Zandi, T. W. Hamann, *J. Phys. Chem. Lett.* **2014**, *5*, 1522–1526.
[35] C. Du, X. G. Yang, M. T. Mayer, H. Hoyt, J. Xie, G. McMahon, G. Bischoping, D. W. Wang, *Angew. Chem. Int. Ed.* **2013**, *52*, 12692–12695.
[36] G. J. Brug, A. L. G. Vandeneeden, M. Sluytersrehbach, J. H. Sluyters, *J. Electroanal. Chem.* **1984**, *176*, 275–295.
[37] R. L. Spray, K. J. McDonald, K. S. Choi, *J. Phys. Chem. C* **2011**, *115*, 3497–3506.

© 2014 WILEY-VCH Verlag GmbH & Co. KGaA, Weinheim